Rupture directivity from energy envelope deconvolution: theory and application to 69 Ridgecrest M 3.5–5.5 earthquakes

Zhe Jia[1], Peter M. Shearer[1], and Wenyuan Fan[1]

[1]Scripps Institution of Oceanography, UC San Diego, La Jolla, California, USA

Key Points:

- We develop an energy envelope deconvolution method to resolve small earthquake rupture directivities.
- Directivities of 69 Ridgecrest earthquakes reveal a complex interlocked fault system.
- Spatial patterns of the directivity estimates appear to correlate with heterogeneity in earthquake stress drops.

Corresponding author: Zhe Jia, `z5jia@ucsd.edu`

Abstract

Earthquake rupture directivity impacts ground motions and provides important insights on fault zone properties and earthquake physics. However, measuring directivity of small earthquakes is challenging due to their compact rupture sizes and complex path and site effects at high frequencies. Here, we develop a new approach that deconvolves energy envelopes of the S-coda waves to remove path and site effects and robustly resolve azimuthal variations in apparent source-time functions. Our method benefits from the coherence of energy envelopes for high-frequency seismic data, which provides more stable directivity results than regular deconvolution methods. We validate our method using synthetic tests and a well-documented moderate-sized event. We apply the algorithm to determine rupture directivities of 69 magnitude 3.5–5.5 earthquakes during the 2019 Ridgecrest earthquake sequence. The rupture directivities suggest an orthogonal interlocking fault system consistent with aftershock locations. Additionally, the rupture directivity pattern appears to correlate with spatial heterogeneity in earthquake stress drops. Our energy envelope deconvolution method enables directivity measurements at lower magnitudes than traditional approaches and has potential for constraining small earthquake rupture dynamics.

Plain Language Summary

Earthquake faults often rupture in a single direction, which can be detected by measuring the "Doppler" shift in their seismic radiation, i.e., that seismic stations in the direction of rupture record shorter pulses than those observed at other stations. These directivity effects are easily seen for large earthquakes but are challenging to measure for small events because their apparent pulse widths are biased by scattering from small-scale crustal structure. Here we develop a new approach that uses seismogram envelope functions rather than the original records and show that it provides more robust directivity results than more standard methods. Application to 69 aftershocks of the 2019 Ridgecrest earthquakes reveals a complex network of faulting behavior.

1 Introduction

Rupture directivity leads to asymmetries in the duration and intensity of seismic radiation around faults and is seen most clearly for unilateral ruptures with a single preferred rupture direction. Directivity causes variations in ground motion intensity and frequency content, thereby affecting the seismic hazard distribution near faults [*Somerville et al.*, 1997; *Kurzon et al.*, 2014]. Moreover, large earthquakes often involve geometrically complex faults, which may include junctions, kinks, and interlocked branches [*Wang et al.*, 2018; *Jia et al.*, 2020a, 2023]. The mechanical properties of these complex fault systems and their earthquake rupture properties are related to rupture directivity. For example, numerical models suggest that slip along a bimaterial interface favors rupture directivity aligned with slip in the more compliant medium [*Zaliapin and Ben-Zion*, 2011; *Andrews and Ben-Zion*, 1997], and directivity can also be influenced by heterogeneous prestress distributions [*Harris and Day*, 2005; *Wang and Rubin*, 2011] and fluid migration along the fault interface [*Folesky et al.*, 2016; *Yoshida et al.*, 2022].

Rupture directivity is usually constrained based on differences in the source duration and amplitude of seismic waves across stations at different azimuths [*Tan and Helmberger*, 2010; *Kane et al.*, 2013a]. Large earthquakes often show asymmetric rupture propagation [*McGuire et al.*, 2002], and their rupture directivity can be resolved with various methods, including back projection [*Fan and Shearer*, 2016; *Ishii et al.*, 2005], finite fault inversion [*Ji et al.*, 2002; *Hartzell and Heaton*, 1983], second moments [*McGuire et al.*, 2001], and subevent modeling [*Kikuchi and Kanamori*, 1991; *Jia et al.*, 2020b]. However, large events occur infrequently in any given region and thus the more abundant small magnitude earthquakes are better suited to image fault systems. The durations and spectra of body waves are commonly used to estimate the rupture directivity of small earthquakes [*Boore and Joyner*, 1978; *Warren and Shearer*, 2006; *Cesca et al.*, 2011]. Small earthquakes have compact fault areas, challenging conventional modeling approaches, as resolving their rupture directivities requires analyzing high-frequency seismic waves at wavelengths matching their rupture sizes. However, existing seismic velocity models face challenges in capturing small-scale heterogeneity at frequencies higher than about 0.2 Hz [*Lee et al.*, 2014; *Wang et al.*, 2024] and using inaccurate velocity models can introduce errors in earthquake source characterizations [*Luo et al.*, 2010; *Graves and Wald*, 2001; *Frohlich and Davis*, 1999]. As a result, systematic investigations into rupture directivities of small earthquake have been rare.

A common approach to determine rupture directivity without knowing all the details of the seismic velocity structure is the empirical Green's function (EGF) method, which assumes that seismic wave propagation effects from co-located earthquakes are similar regardless of their source processes. In this approach, the seismic waves of a small earthquake, termed the EGF event, can be used to model a nearby larger event, with the shared path and site effect removed through waveform deconvolution [*Hartzell*, 1978; *Mueller*, 1985; *Hough*, 1997]. However, the seismic radiation of smaller earthquakes is dominated by high frequencies, and EGF deconvolution of small earthquakes faces challenges of cycle skipping because high-frequency waves are more prone to phase misalignment in the deconvolution process [*Li and Nábělek*, 1999; *Vallée et al.*, 2011]. Moreover, the prevalence of scattered waves at high frequencies can further obscure the source-time functions retrieved from deconvolution. These factors hamper accurate determination of rupture directivity and the application of the EGF method to smaller magnitude earthquakes [*Mueller*, 1985; *Vallée*, 2004].

Here, we apply a new energy-envelope deconvolution method to robustly determine small earthquake horizontal rupture directivities. Instead of traditional approaches focusing on the seismic waves directly, our method involves deconvolution of energy envelopes of S waves for pairs of seismic events to remove path effects and extract rupture characteristics. Our approach benefits from better coherency of energy envelopes at high frequencies [*Nakahara et al.*, 1998; *Wu et al.*, 2014], thereby enhancing the robustness of the source-time-function estimation and rupture directivity determination. We validate our energy deconvolution analysis using synthetic examples and a well-studied moderate-sized event. We apply the algorithm and determine unilateral rupture directivities of 69 magnitude (M) greater than 3.5 events during the 2019 Ridgecrest earthquake sequence. Our results suggest a complex interlocked fault system, which likely modulates the earthquake faulting processes and impacts earthquake rupture dynamics.

2 Methods

2.1 Energy envelope inversion framework

Considering the Earth as a linear system for seismic wave propagation, the observed seismic waves $u(t)$ for an earthquakes can be represented as $u(t) = S(t) * G(t)$, where $S(t)$ represents the source time function, $G(t)$ is the Green's function, and $*$ is the convolution operator. Conventional waveform deconvolution assumes the source-time function of the smaller event in an earthquake pair to be a simple pulse, which can be approximated as a delta function when the waveform frequencies are below its corner frequency. This assumption allows for the recorded waveforms of the smaller event to be effectively approximated as $G(t)$. Consequently, the deconvolution of the waveforms can remove the common path term $G(t)$ and retrieve the source-time function of the larger target event.

This workflow is also applicable to envelopes of high-frequency waves, assuming the high frequency source-time functions are mutually uncorrelated and consist of narrowband random scattered waves [*Nakahara*, 2008; *Sato et al.*, 2012]. The energy envelope function of the seismic waves can be expressed as $< u^2(t) >=< S^2(t) > * < G^2(t) >$, where $<>$ indicates the envelope function of the time series. Assuming the smaller event's source is a delta function, we can approximate its energy envelope waveforms as envelope Green's functions $< G^2(t) >$, and employ EGF deconvolution to isolate the energy-envelope source-time functions. Envelope deconvolution is particularly suitable for high-frequency seismic data for small earthquakes, as envelopes not only keep the high-frequency information of the source but also retain the coherency of retrieved source-time functions across different stations. The duration of this energy-envelope source-time function is the same as that of earthquake apparent-source-time function, enabling directivity analysis.

To demonstrate the concept of energy-envelope deconvolution, we perform a numerical test (Fig. 1). We generate synthetic source-time functions for a pair of seismic events. For the smaller EGF event, we employ a delta function as its source-time function. For the larger target event, we design its source-time function using a combination of a Hann pulse (12-s duration), a half sine wave (8-s duration), and normally distributed random noise, aiming to mimic a complex rupture history of the larger event. For the Green's function, we use an exponential decay function with a characteristic duration of 3 seconds, again including normally distributed random noise to simulate high-frequency scattered waves. We then generate synthetic waveforms for both events by convolving their source time functions with the simulated Green's function. Using these synthetic time series, we compare standard deconvolution with energy-envelope deconvolution. Standard deconvolution fails to resolve the duration of the target event, while the envelope deconvolution method can recover the input source duration. This exercise illustrates the effectiveness of energy envelope deconvolution.

Our procedure focuses on resolving the horizontal rupture directivity. Both horizontal and vertical rupture directivity can influence the spatial distribution of the apparent source-duration pattern. The horizontal directivity is reflected in the azimuthal variation of the apparent duration, while the vertical directivity is mostly related to the take-off angles [*Tan and Helmberger*, 2010; *Cesca et al.*, 2011; *Mori*, 1996]. For the Ridgecrest earthquakes, their shallow depths and a relative lack of stations above them lead to the recorded S waves having mostly near-horizontal take-off directions, which limits resolving the vertical rupture directivity.

For the deconvolution, we use a non-negative least-squares (NNLS) inversion [*Bro and De Jong*, 1997] to obtain positive energy source-time functions. In the NNLS inversion, we adopt a regularization scheme that uses the azimuthal gap of the stations [*Ekström*, 2006; *Jia and Clayton*, 2021], include a corresponding exponential penalty term to the cost function to penalize incoherent apparent source-time functions at close azimuths. The characteristic azimuthal gap is set to be 20 degrees. After we obtain the energy source-time functions, we estimate the apparent source duration for each source-time-function trace. This is achieved by defining the ending point where the amplitude decreases to 30% of the peak amplitude of the source-time function. Variations in these apparent source durations reflect the Doppler effect generated by unilateral rupture directivity, and we apply linear regression to these apparent source durations to invert the source parameters including the source duration, rupture direction, and rupture velocity. As the resolved rupture directivities should be consistent with the focal mechanisms, we employ a constraint that the search for rupture directivity is among the four nodal strikes, to obtain the solution that best fits the apparent source durations.

2.2 Composite earthquake test

The coherence of energy envelopes significantly enhances the robustness of obtaining the energy source-time function, thereby improving the rupture directivity estimation. As a demonstration, we conduct a second test, using two real earthquakes recorded at regional distances (Fig. 2). We use a time window 0.5 s before, and 5 s after, the predicted onset of the SH waves [*White et al.*, 2021], and filter the waveforms between 5 and 10 Hz. We synthesize a complex M_W 3.9 earthquake by combining the waveforms of a M_W 3.65 event (as the first subevent, SCEDC ID 38451239) with those from a closely located M_W 3.72 event (as the second subevent, SCEDC ID 38448791), both from the 2019 Ridgecrest earthquake sequence, and apply different time shifts across stations corresponding to a northeastward horizontal rupture directivity (55°) at 1.5 km/s, with a separation distance of 1.5 km (1 seconds separation). We use the M_W 3.65 earthquake as an EGF event. The composite waveforms show clear onset phases of the first subevent, but the second subevent's contributions are notably contaminated by the coda waves of the first subevent.

Using these synthetic waveform data, we compare conventional deconvolution and energy envelope deconvolution in determining the rupture directivity for the synthesized M_W 3.9 event.

Apparent source-time functions from conventional deconvolution show coherent phases for the initial subevent. However, they are followed by multiple peaks that complicate identification of the second subevent. The estimated source durations cannot resolve the horizontal rupture directivity and the best-fitting rupture directivity deviates from the input configuration (Fig. 3). In contrast, the apparent source-time functions derived from energy envelope deconvolution show coherent azimuthal patterns that clearly delineate both the first and second subevents (Fig. 3). Furthermore, the estimated apparent source durations match the input values, leading to better recovery of the input rupture directivity and highlighting the effectiveness of energy-envelope deconvolution in the directivity analysis of small earthquakes.

3 Application to the 2019 Ridgecrest sequence

Resolving rupture directivity can be very useful in illuminating faulting and the regional stress environment, especially for complex fault networks with multiple active fault strands. For example, the 2019 Ridgecrest earthquake sequence unexpectedly ruptured an orthogonal interlocked fault system [*Ross et al.*, 2019; *Shelly*, 2020; *Lin*, 2020]. We apply the energy envelope deconvolution method to examine the rupture directivity of 165 M_W 3.5–5.5 aftershocks recorded by the Southern California Earthquake Data Center (SCEDC) earthquake catalog [*Center*, 2013]. These events provide uniform spatial coverage of the Ridgecrest faults, which allows high-resolution mapping of rupture styles across the fault network (Fig. 4).

For each M_W 3.5–5.5 target event, we use 10 nearby M_W 2.5–4 EGF earthquakes within a 3D distance of 10 km as EGF events. These EGF events are at least 0.5 magnitude units smaller than their corresponding target events, which is different from the commonly adopted 1 magnitude difference criterion for EGF methods [*Hutchings and Wu*, 1990; *Kane et al.*, 2013b]. We relax the magnitude requirement to increase the number of EGF events and improve their azimuthal coverage, factors we have found more important than obtaining the shortest duration EGF events. These larger magnitude EGF events typically also have higher signal-to-noise ratios. A further advantage is that we are able to lower the minimum magnitude threshold for our target events because it is easier to find suitable EGF events. For both the target and EGF events, we download horizontal component 100 Hz sample-rate broadband data (HH channels) from the Southern California Seismic Network (SCSN) stations within 200-km of the epicenters, then rotate them to radial and transverse components. For each SH wave recorded on the transverse component, we use available S-wave picks that have been reviewed by SCEDC analysts and calculate the theoretical SH arrival times using an averaged 1D velocity model for this region [*White et al.*, 2021] for stations lacking S arrival labels. Similar to the synthetic test, we use a time window 0.5 s before, and 5 s after, the predicted onset of the SH waves, and filter the waveforms between 5 and 10 Hz. We keep the seismograms with a signal-to-noise ratio (SNR) larger than 4 in our deconvolution inversion. The SNR is defined as the ratio of the averaged sum of squares of the signal up to 5 s from the S wave onset, to that of the noise extending 2 s before the onset.

Our target events include a M_W 5.4 earthquake (SCEDC ID 38450263) during the Ridgecrest sequence, which occurred between the M_W 6.4 foreshock and the M_W 7.1 mainshock. This event is located within 2 km epicentral distance of the M_W 7.1 mainshock. Figure 5 shows our energy-envelope deconvolution applied to this M_W 5.4 earthquake, taking a M_W 3.7 earthquake 2 km away as an EGF event (SCEDC ID 38448791). The resolved apparent source-time functions show azimuthally-varying source durations, which translate to a northeastward horizontal rupture directivity of about 50°. Different reference events lead to similar rupture directivity results (Dataset S1). The directivity shows that the M_W 5.4 event ruptured a crosscutting fault striking toward the northeast rather than on the main southeastward fault branch, which is consistent with an independent directivity analysis for this event using the second moments method [*Meng and Fan*, 2021], as well as aligning with the northeast-trending seismicity observed from aftershock relocation [*Shelly*, 2020].

We adopt the constraint that our estimated rupture directivity should agree with one of the focal-mechanism nodal-plane strikes to provide self-consistency on the fault geometry. Removing the focal-mechanism constraint on rupture directivity leads to a similar result for the M_W 5.4 event, because the azimuthal variation of the apparent source durations already constrains the rupture directivity tightly (Fig. 5b,c). This similarity between results from the constrained search and the free search holds for most of the analyzed events (Fig. 6), and the differences are typically within the standard deviation estimated from a bootstrap resampling approach (Fig. 6). Since most of the events in the region are strike-slip earthquakes and their horizontal rupture directions likely align with the fault plane strike, we apply this constraint in our rupture directivity determination for our subsequent analyses. As for the evaluation of the results, we only keep an event pair if the optimal solution has misfit at least 25% smaller than the second-best solution (i.e., from the other three nodal strikes of the focal mechanism). Figure S1 illustrates the case for the M_W 5.4 earthquake example, where the misfit of the optimal rupture directivity is significantly smaller than the misfits for other directivity orientations.

Among all the M_W 3.5–5.5 events analyzed, 69 events are well resolved as unilateral rupture models. The fault geometries inferred from the rupture directivities are consistent with high-resolution aftershock patterns [Fig. 7; *Ross et al.*, 2019]. The ruptures of the 69 earthquakes do not prefer a single direction (Fig. 6a,b). Instead, they exhibit diverse rupture directivity with both NW–SE dominant orientations consistent with the main fault strike, and also NE–SW oriented ruptures cutting across the NE–SW faults (Fig. 6a,b). This variation likely reflects the complexity of the subsurface Ridgecrest faulting environment and stress conditions, suggesting the potential of faults and stress to interact in complex ways during an earthquake, which may influence the rupture duration and final size of earthquakes.

The directivity patterns roughly divide the Ridgecrest fault system into three different subregions (Fig. 7). The northwestern aftershock zone has most of the M 3.5–5.5 event ruptures trending toward the NW–SE, corresponding to subparallel splay faults (Fig. 8). However, there are also 6 events indicating NE-SW trending rupture directivity at different locations, which suggest the existence of multiple active antithetic faults cutting across the NW–SE faults [*Shelly*, 2020; *Wang and Zhan*, 2020]. Ruptures on a few conjugate faults may represent a volumetric strain release through fabric structures, which have been observed in other places and is attributed to the presence of fluids [*Toda and Stein*, 2003; *Ross et al.*, 2017; *Kato et al.*, 2021].

The middle segment corresponds to faults near the M_W 7.1 earthquake epicenter and its largest slip patch [*Ross et al.*, 2019; *Jia et al.*, 2020a]. Although the surface ruptures have two main traces with along-strike variations, most aftershocks rupture along a narrow straight band trending NW–SE (Fig. 9). Aftershocks that rupture along NE–SW directions are relatively clustered and indicate the existence of three minor sub-faults cutting across the NW–SE main fault strand. The rupture directivities, surface rupture traces, and the relocated seismicity collectively suggest that the shallow subparallel fault segments are likely connected by a deeper through-going fault, forming a flower fault structure. This superficially complex but simpler through-going fault geometry at depth is supported by flower structures imaged from seismic reflections in the region [*Monastero et al.*, 2002], and is consistent with refined aftershock focal mechanisms [*Wang and Zhan*, 2020] and slip models [*Jia et al.*, 2020a; *Jin and Fialko*, 2020].

Earthquakes in the southeastern section exhibit highly variable rupture directivities. These rupture directivities show significant fault geometrical variations (Fig. 10). For example, the main through-going fault bifurcates into several sub-parallel horsetail splays. There is also a series of conjugate faults cutting across these splay faults, which include the main NE–SW trending fault ruptured by the M_W 6.4 foreshock. These horsetail faults and interlocked fault segments correspond to the southeastern end of the M_W 7.1 mainshock, where the rupture stopped only a few kilometers from the Garlock fault [*Ross et al.*, 2019].

4 Discussion and conclusions

We develop an energy envelope deconvolution method to measure apparent-source durations and resolve rupture directivities of small earthquakes. One limitation of our approach, in common with many directivity studies, is that it cannot determine bilateral rupture or weak rupture directivity. Our analysis considers 165 M_W 3.5–5.5 events, but after removing events with low signal-to-noise ratios and insignificant misfit reduction, we obtain only 69 earthquakes that show clear unilateral rupture directivity. For a bilateral rupturing earthquake, the apparent-source durations across different stations will have two lobes of minimum duration in opposite directions, instead of a single lobe in the rupture direction as in the case of unilateral rupture [*Cesca et al.*, 2011; *Calderoni et al.*, 2017]. Constraining bilateral rupture components for an individual event requires dense azimuthal coverage of stations, as substantial azimuthal gaps will obscure the two lobes and challenge the rupture directivity determination. Omitting bilateral ruptures may lead to resolving only the stronger rupture direction as unilateral rupture directivity, which could explain the observed low horizontal rupture velocities between 1.0–2.5 km/s for the analyzed Ridgecrest events (Fig. 11).

Our directivity results indicate a complex faulting and stress environment, agreeing with details in the aftershock locations, which varies across the Ridgcrest fault zone. The fault architecture at the northwestern and southeastern sections shows remarkable complexity with numerous subsidiary fault segments and fault junctions, whereas the middle segment appears smoother and simpler. We quantify the variation of fault strikes inferred from rupture directivities, using the standard deviation of the fault strikes within distance bins of 5-km radius, and compare them with small earthquake stress drops independently estimated using a spectral decomposition method [*Shearer et al.*, 2022]. We find that the central section with the simpler fault geometry has earthquakes with higher average stress drops, while earthquakes occurring in the complex northwestern and southeastern sections have lower average stress drop values (Fig. 12). This correlation between fault simplicity inferred from our results and stress drop also appears to align with the largest slip occurring in the central segment of Ridgecrest faults during the M_W 7.1 mainshock [*Jia et al.*, 2020a; *Ross et al.*, 2019; *Wang et al.*, 2020].

This observation seems counter-intuitive, as the existence of fault geometrical complexities and damage zones are often associated with higher strain accumulation over time, leading to higher-frequency seismic radiation when rupture occurs, both of which lead to higher stress drops [*Aki*, 1979; *Chu et al.*, 2021]. Our observations might be related to fault-complexity-induced barriers along the fault, which could stall the earthquake rupture development and confine small earthquakes within weak patches, leading to smaller slip amounts and partial stress releases [*Das and Aki*, 1977; *Nielsen and Knopoff*, 1998; *Zielke et al.*, 2017]. In this case, smooth fault surfaces such as the central segment of the Ridgecrest fault system allow earthquakes to develop in similar ways, leading to less variation in rupture directivity [*Thakur and Huang*, 2021; *Xu et al.*, 2023]. Our directivity observations for the central Ridgecrest fault section qualitatively agree with the stress-drop variations. However, the aforementioned competing mechanisms allow faulting-environment complexity to have the potential to both increase and decrease stress drops, and the overall effect might also depend on smaller-scale rheological or stress heterogeneities [*Kane et al.*, 2013a; *Goebel et al.*, 2015; *Meng and Fan*, 2021].

Complex faulting environments play a critical role in controlling earthquake rupture dynamics, as they allow diverse rupture trajectories, such as unexpected cascades and fault-to-fault jumps [*Hamling et al.*, 2017; *Ross et al.*, 2019; *Jia et al.*, 2023]. However, this complexity often remains unresolved until a large earthquake occurs and illuminates the fault geometry. In this case, multi-fault ruptures can extend the total rupture length and seismic moment, and conventional hazard assessments may underestimate the maximum potential earthquake magnitude by neglecting these phenomena [*Schwartz et al.*, 2012; *Nissen et al.*, 2016; *Iacoletti et al.*, 2021]. Our energy envelope deconvolution method has the capability to extend directivity analyses to smaller earthquakes, thus expanding the number of events for which results can be obtained, and better illuminating the complexities of fault networks. This understanding of the geometry of faults and their intersections could aid in assessing additional seismic hazards brought by multi-fault rupture scenarios that involve blind, buried, or poorly exposed fault systems.

Acknowledgments

We thank the Southern California Earthquake Data Center (SCEDC) [*Center*, 2013] for providing public access to all the Southern California Seismic Network (SCSN) near-field seismic data used in this study. This work is supported by the United States Geological Survey grant G22AP00011, and the Cecil and Ida Green Foundation.

Open Research

All waveform data are publicly available from the Caltech/USGS Southern California Seismic Network and through the STP software [*Center*, 2013]. The SCEDC focal mechanism catalog is available at the SCEDC search portal [*Center*, 2013]. Some figures are generated using the Generic Mapping Tools Software [*Wessel et al.*, 2013].

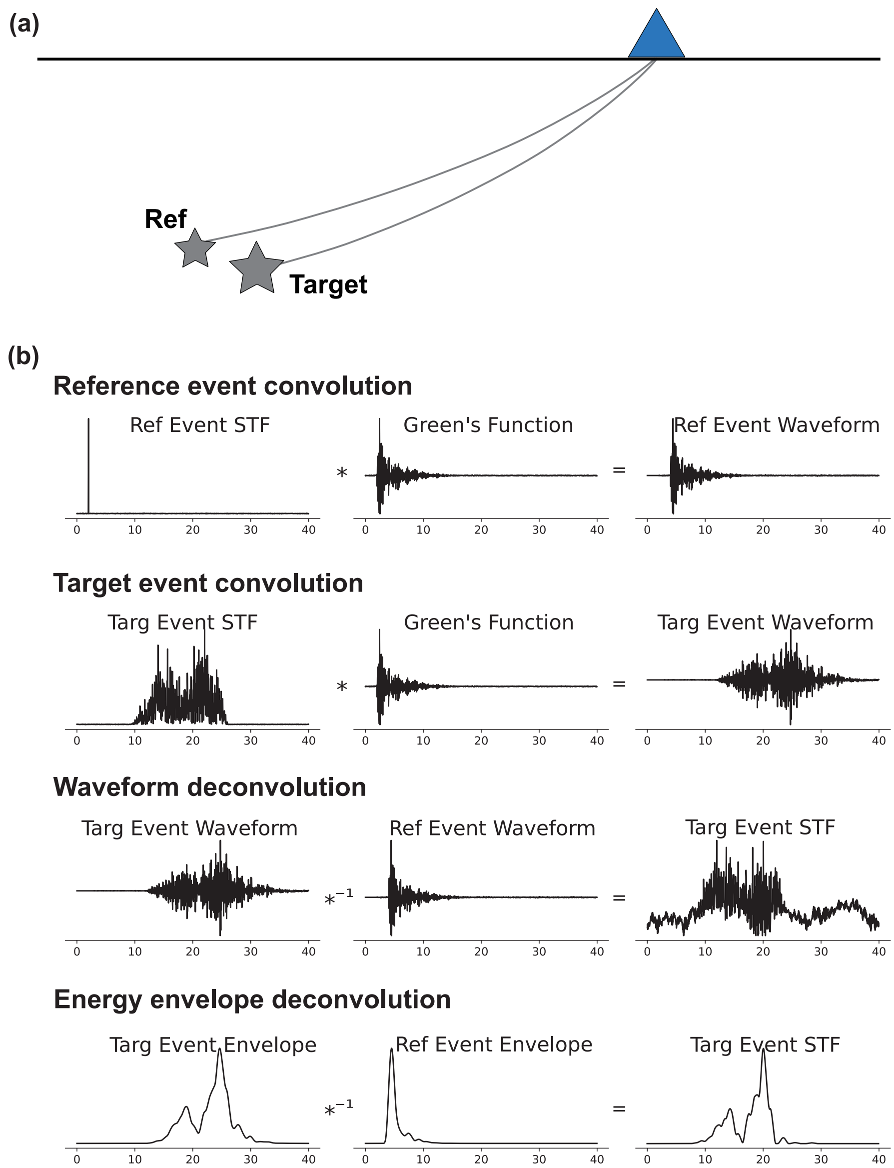

Figure 1. Illustration of the energy envelope deconvolution method. (a) Empirical Green's Function (EGF) reference events are smaller seismic events that have similar locations and path and site effects compared to larger target events. (b) Taking the reference event waveform as a proxy for the Green's function, we can obtain the source time function (STF) of the target event by deconvolving the target event waveform with the reference event's waveform, as indicated by the first two rows. Compared to waveform deconvolution (third row), deconvolution of energy envelopes (fourth row) better preserves the shape of the two subevents in the STF of the target event.

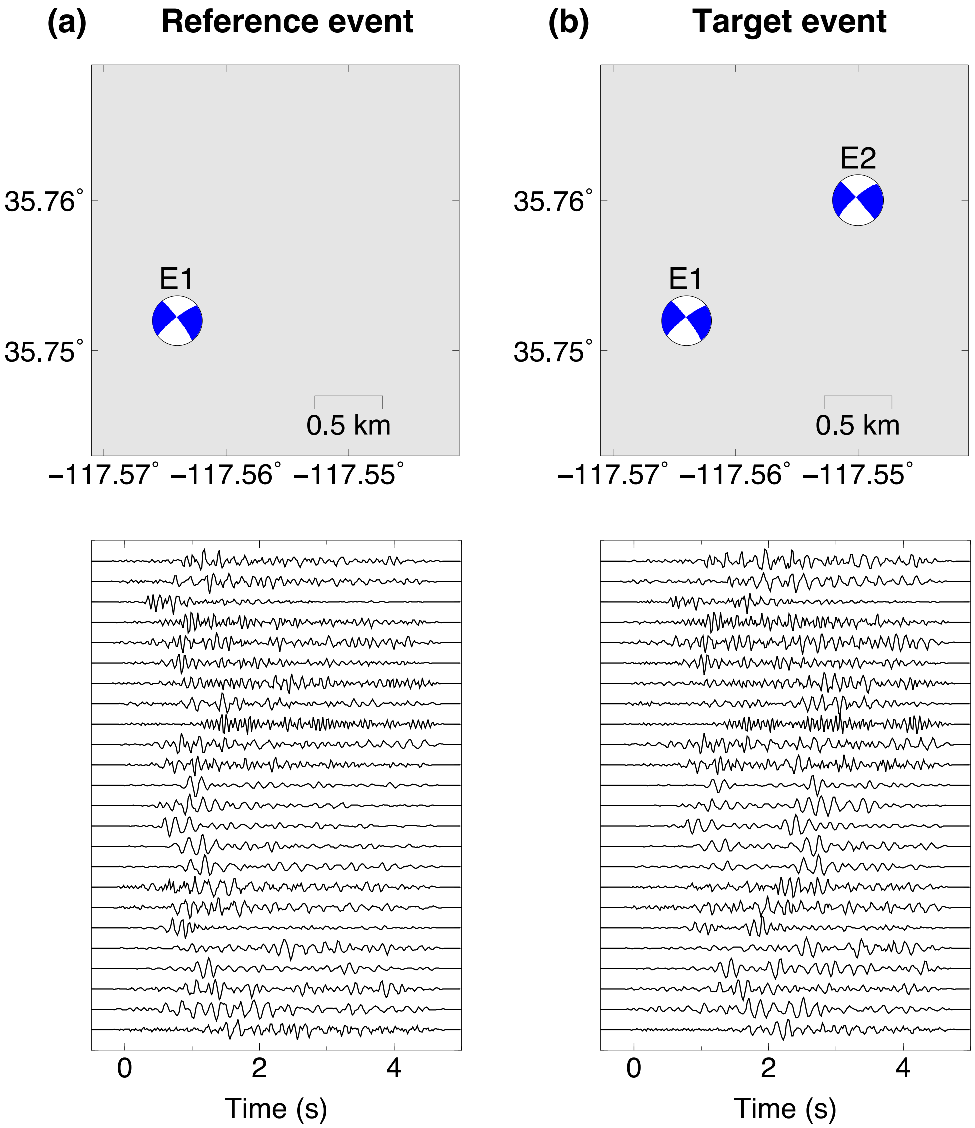

Figure 2. Composite reference and target event formed using real earthquake data. (a) The reference event, a M_W 3.65 Ridgecrest earthquake (SCEDC id 38451239), with location and focal mechanism indicated by the blue beachball in the upper panel. The lower panel shows transverse-component shear waves of this event sorted by station azimuth. (b) Target event synthesized by summing the waveforms from the M_W 3.65 event (SCEDC id 38451239) for the first subevent and a second M_W 3.72 event (SCEDC id 38448791) for the second subevent. We applied time shifts for these two subevents corresponding to a time delay of 1.5 s and a relative distance of 1.5 km, to simulate northeastward rupture directivity. Note that the waveforms from the two subevents have overlaps and interfere at most stations.

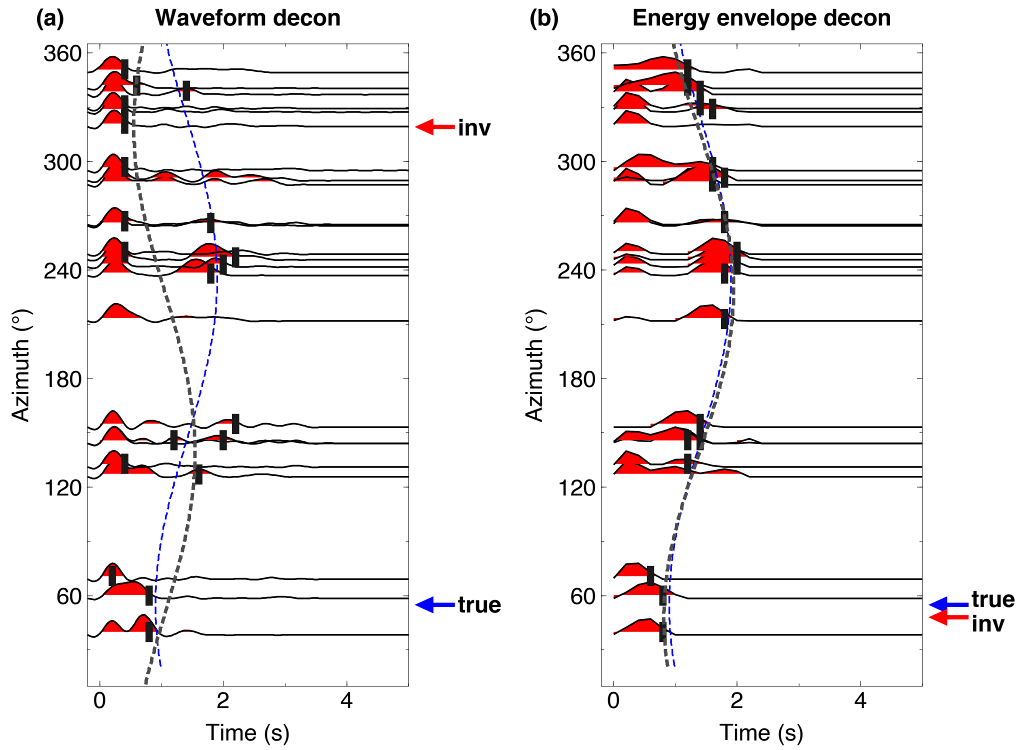

Figure 3. Comparison of source-time functions of the composite target event (Fig. 2) derived from: (a) waveform deconvolution, and (b) energy envelope deconvolution. The vertical black dashes show the limit for measuring apparent source durations. The dashed gray and blue lines indicate the best fit and true source duration curves in each scenario, respectively. Red and blue arrows denote the inverted and true rupture directivities, respectively.

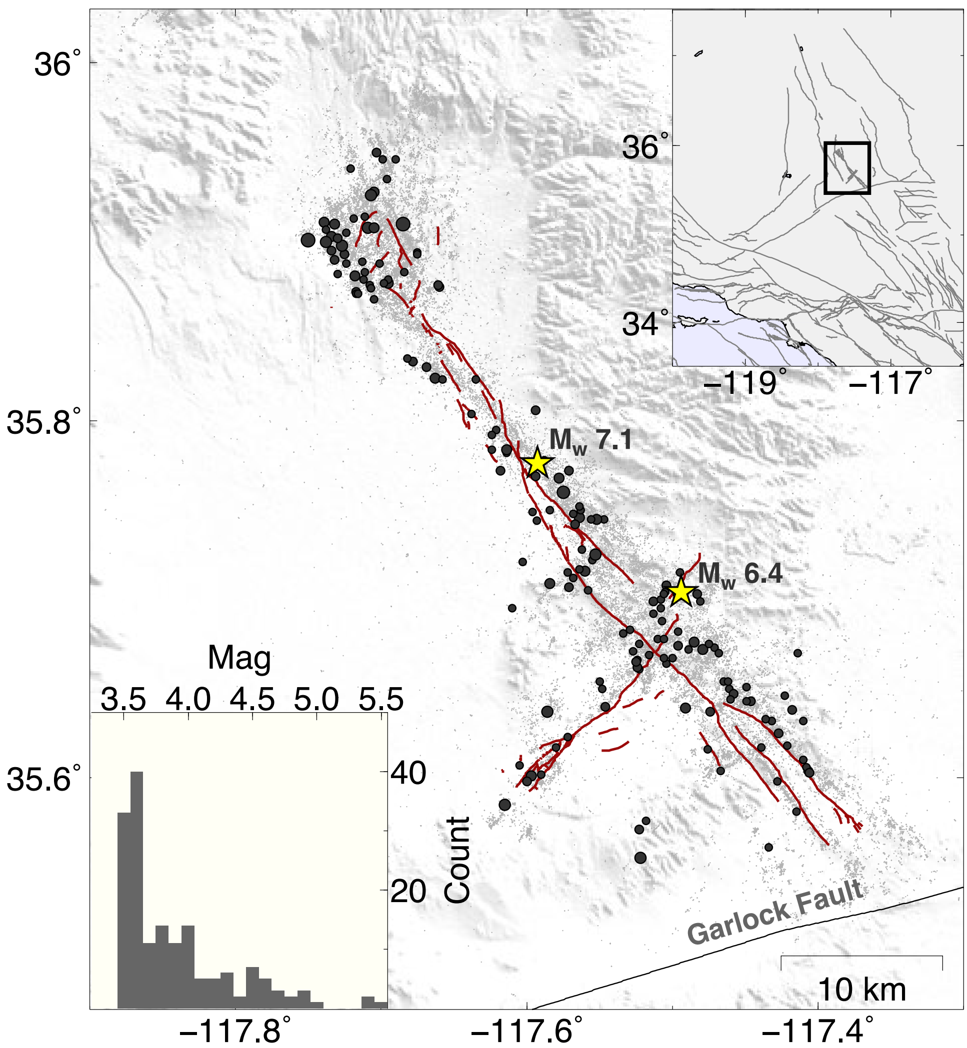

Figure 4. Seismicity of the Ridgecrest region. The red lines indicate the mapped surface ruptures [*Brandenberg et al.*, 2020]. Light gray dots indicate relocated aftershocks [*Ross et al.*, 2019], among which the dark gray circles are earthquakes analyzed in this study, with magnitudes between 3.5 and 5.5. Lower right inset histogram shows the magnitude distribution of these events. Upper left inset show the location of the map on a larger-scale California fault map.

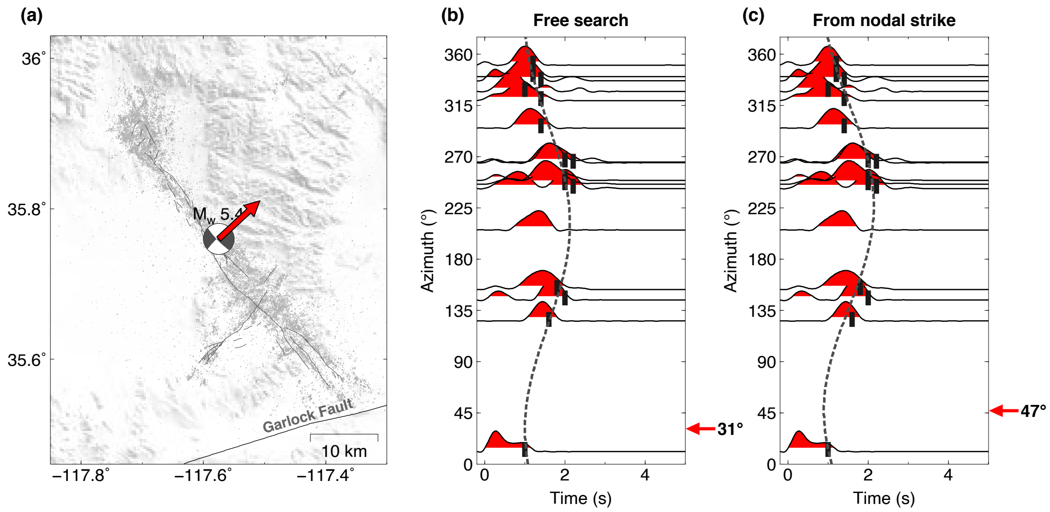

348 **Figure 5.** Energy envelope deconvolution of the 2019 M_W 5.4 Ridgecrest earthquake. (a) Resolved rupture directivity of the M_W 5.4 event indicated by the red arrow. We use the magnitude 3.72 earthquake (SCEDC id 38448791) as a reference event in the deconvolution processes. (b) Rupture directivity estimated permitting all possible directions. (c) Rupture directivity derived with the constraints that the directivity should be consistent with the focal mechanism strike angles.

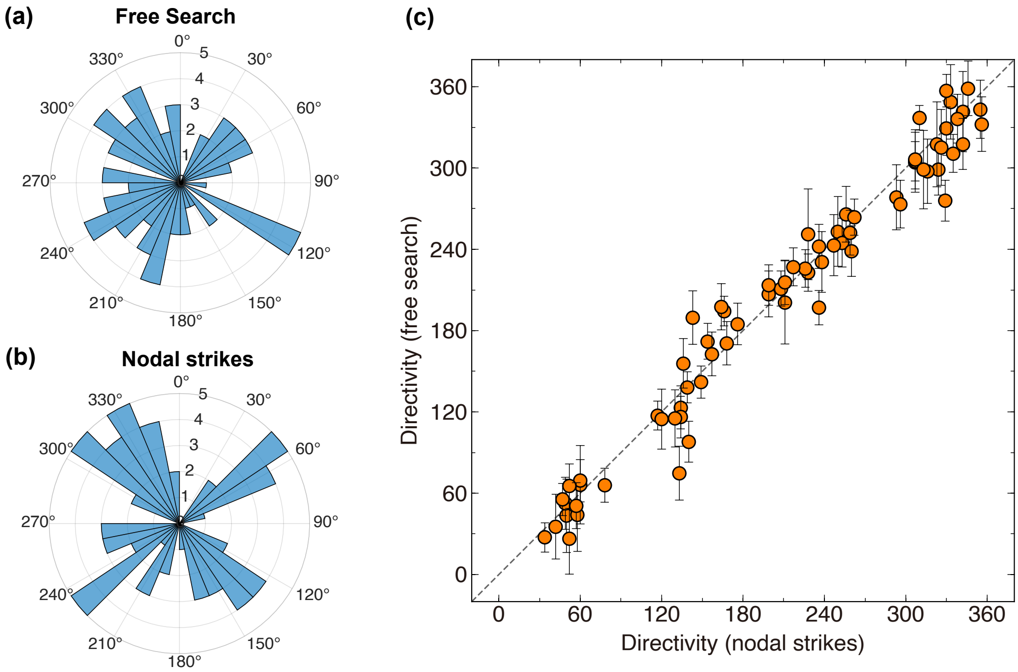

Figure 6. Comparison between directivity results of 69 events from the free and nodal-strike-constrained searches. (a) Rose diagram of the rupture directivities from the unconstrained searches. (b) Rose diagram of the rupture directivities from inversions that align the directivities with focal mechanism nodal strikes. Maximum radius denotes five events. (c) Comparison of the directivity results for the free and constrained searches. The error bars indicate the standard deviations of the free-searched directivities, derived using a bootstapping resampling approach.

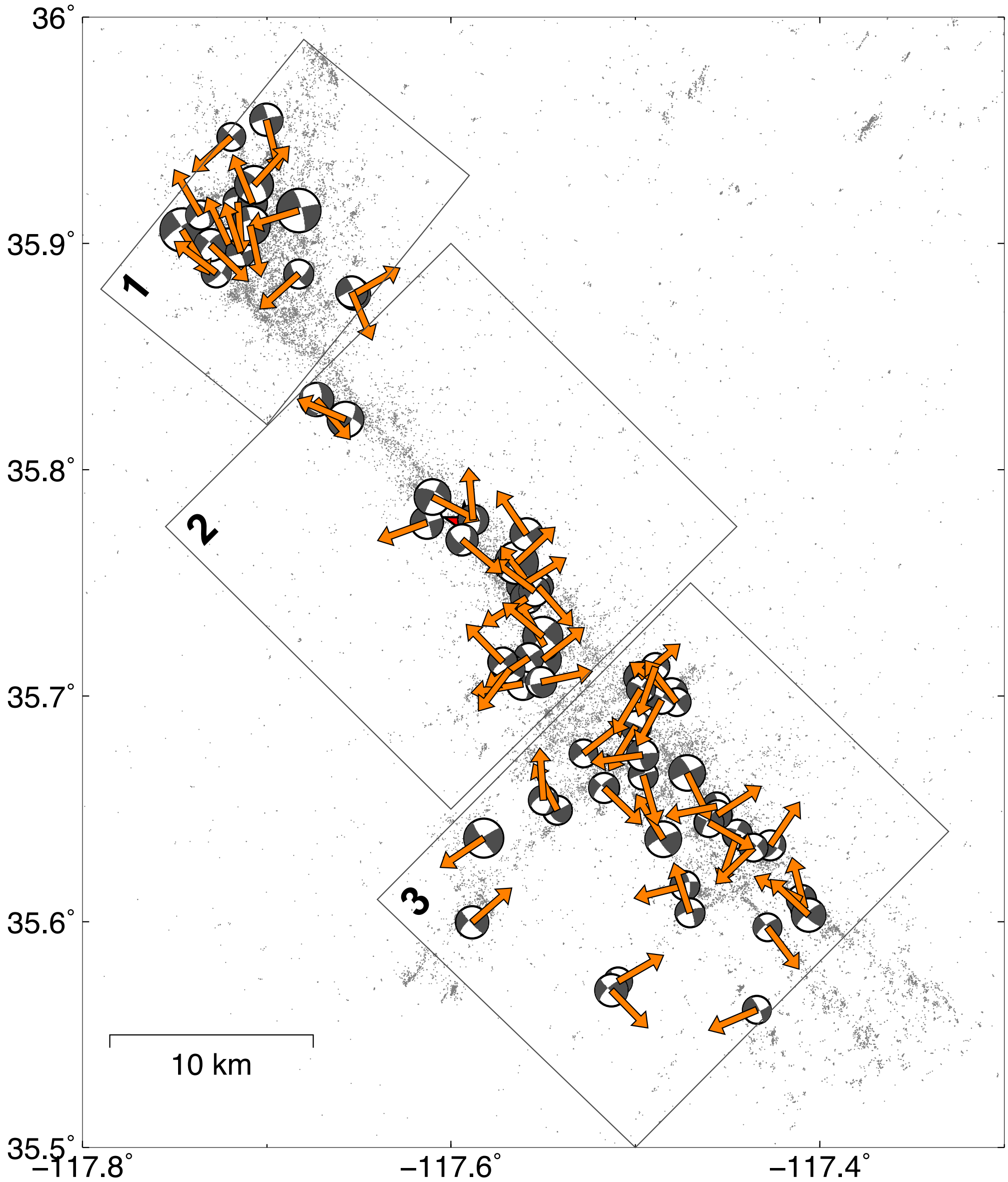

359 **Figure 7.** Spatial distribution of the rupture directivities of 69 M_W 3.5–5.5 earthquakes. Directivities are
360 shown by the orange arrows on corresponding beachballs. Inset rectangles show three sub-regions of the
361 Ridgecrest fault system shown in Figs. 8–10.

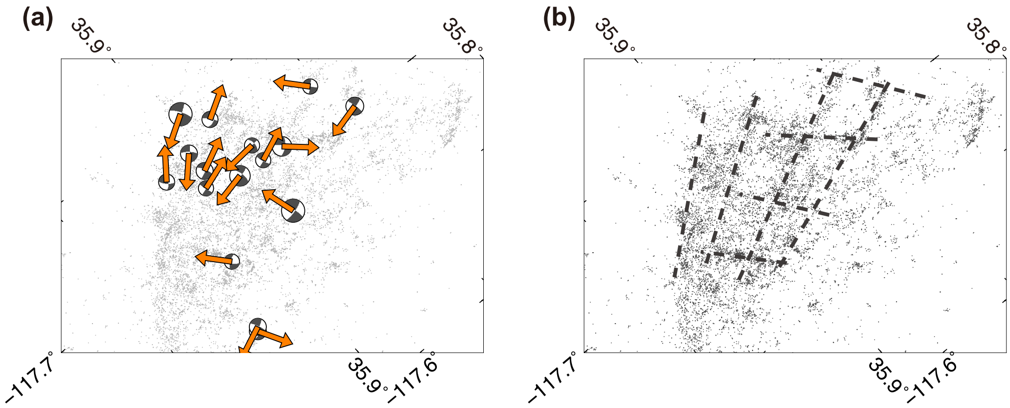

Figure 8. Rupture directivities of earthquakes in the northwestern section of the Ridgecrest fault system (a), and inferred fault architecture from seismicity (b). The inferred faults as shown by dashed lines align well with the aftershock locations (gray dots). The northwestern section exhibits complex subparallel splay faults with a few antithetic faults cutting across them.

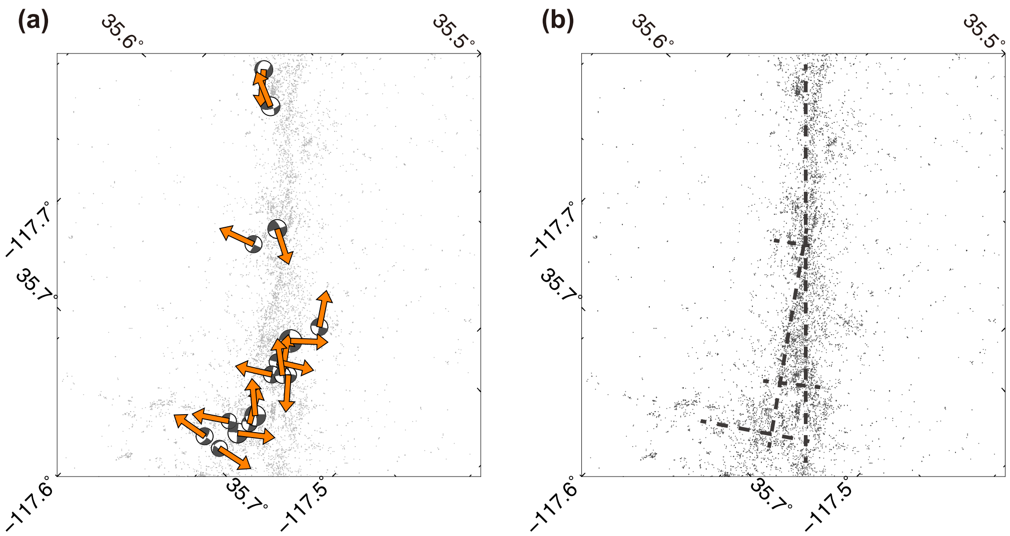

366 **Figure 9.** Middle section of the Ridgecrest fault system. Symbols are the same as Fig. 8. The middle
367 section consists two major subparallel NW-SE fault segments with three smaller NE-SW oriented subfaults
368 cutting across them.

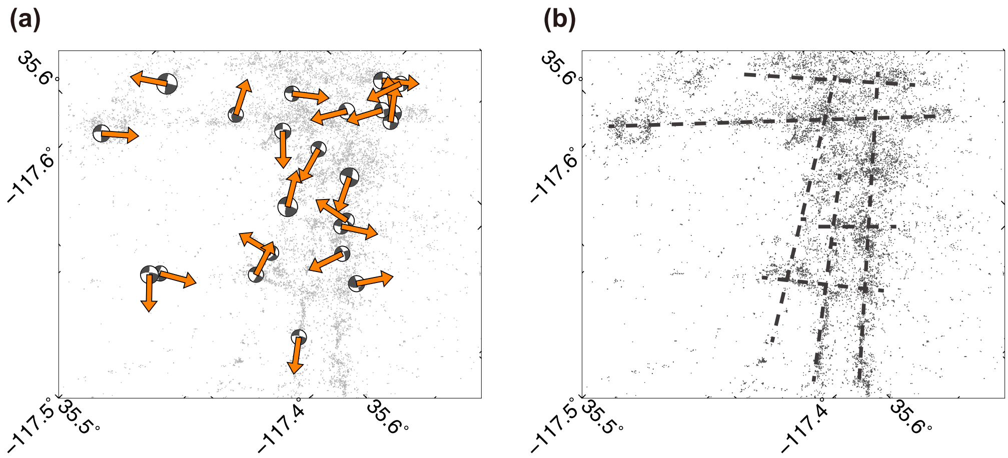

Figure 10. Southeastern section of the Ridgecrest fault system. Symbols are the same as in Fig. 8. The rupture directivities are highly variable, and the inferred fault lines suggest complex fault bifurcation into multiple horsetail lines with a number of NE-SW trending subfaults cutting across them.

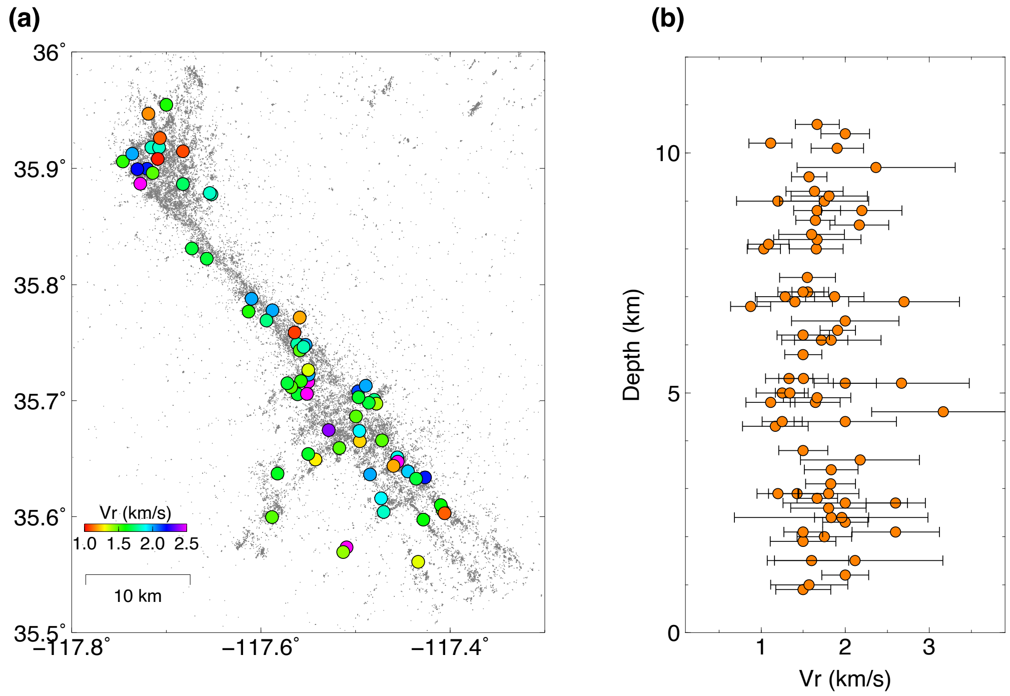

372 **Figure 11.** Distribution of rupture velocities. (a) Rupture velocities of the analyzed Ridgecrest events shown by the colored circles. (b) Depth distribution of rupture velocities. We do not observe significant depth-dependence of these rupture velocities.

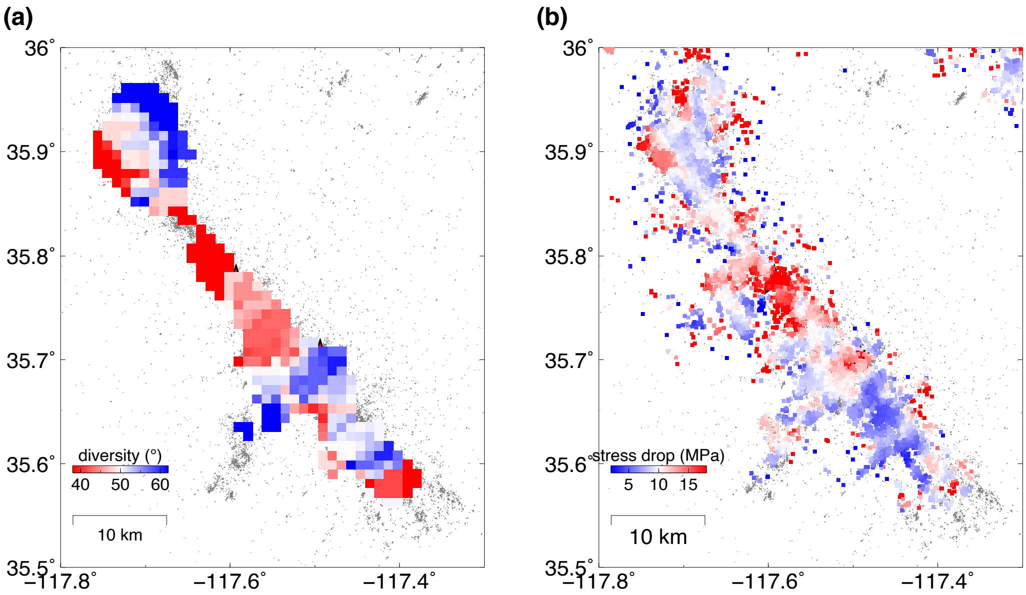

375 **Figure 12.** Comparison between fault strike variation with small earthquake stress drops. (a) Standard
376 deviation of the fault strike orientations, calculated using earthquakes within 5-km distance radius for each
377 event. (b) Stress drop estimates for M 1.5 to 4 earthquakes in the Ridgecrest region [*Shearer et al.*, 2022].

References

Aki, K. (1979), Characterization of barriers on an earthquake fault, *Journal of Geophysical Research: Solid Earth*, *84*(B11), 6140–6148.

Andrews, D. J., and Y. Ben-Zion (1997), Wrinkle-like slip pulse on a fault between different materials, *Journal of Geophysical Research: Solid Earth*, *102*(B1), 553–571.

Boore, D. M., and W. B. Joyner (1978), The influence of rupture incoherence on seismic directivity, *Bulletin of the Seismological Society of America*, *68*(2), 283–300.

Brandenberg, S. J., J. P. Stewart, P. Wang, C. C. Nweke, K. Hudson, C. A. Goulet, X. Meng, C. A. Davis, S. K. Ahdi, M. B. Hudson, et al. (2020), Ground deformation data from GEER investigations of Ridgecrest earthquake sequence, *Seismological Research Letters*, *91*(4), 2024–2034.

Bro, R., and S. De Jong (1997), A fast non-negativity-constrained least squares algorithm, *Journal of Chemometrics: A Journal of the Chemometrics Society*, *11*(5), 393–401.

Calderoni, G., A. Rovelli, and R. Di Giovambattista (2017), Rupture directivity of the strongest 2016–2017 central Italy earthquakes, *Journal of Geophysical Research: Solid Earth*, *122*(11), 9118–9131.

Center, E. (2013), Southern California earthquake center, *Caltech. Dataset*.

Cesca, S., S. Heimann, and T. Dahm (2011), Rapid directivity detection by azimuthal amplitude spectra inversion, *Journal of seismology*, *15*, 147–164.

Chu, S. X., V. C. Tsai, D. T. Trugman, and G. Hirth (2021), Fault interactions enhance high-frequency earthquake radiation, *Geophysical Research Letters*, *48*(20), e2021GL095,271.

Das, S., and K. Aki (1977), Fault plane with barriers: A versatile earthquake model, *Journal of geophysical research*, *82*(36), 5658–5670.

Ekström, G. (2006), Global detection and location of seismic sources by using surface waves, *Bulletin of the Seismological Society of America*, *96*(4A), 1201–1212.

Fan, W., and P. M. Shearer (2016), Local near instantaneously dynamically triggered aftershocks of large earthquakes, *Science*, *353*(6304), 1133–1136.

Folesky, J., J. Kummerow, S. A. Shapiro, M. Häring, and H. Asanuma (2016), Rupture directivity of fluid-induced microseismic events: Observations from an enhanced geothermal system, *Journal of Geophysical Research: Solid Earth*, *121*(11), 8034–8047.

Frohlich, C., and S. D. Davis (1999), How well constrained are well-constrained T, B, and P axes in moment tensor catalogs?, *Journal of Geophysical Research: Solid Earth*, *104*(B3), 4901–4910.

Goebel, T., E. Hauksson, P. Shearer, and J. Ampuero (2015), Stress-drop heterogeneity within tectonically complex regions: A case study of San Gorgonio Pass, southern California, *Geophysical Journal International*, *202*(1), 514–528.

Graves, R. W., and D. J. Wald (2001), Resolution analysis of finite fault source inversion using one-and three-dimensional Green's functions: 1. Strong motions, *Journal of Geophysical Research: Solid Earth*, *106*(B5), 8745–8766.

Hamling, I. J., S. Hreinsdóttir, K. Clark, J. Elliott, C. Liang, E. Fielding, N. Litchfield, P. Villamor, L. Wallace, T. J. Wright, et al. (2017), Complex multifault rupture during the 2016 M w 7.8 Kaikōura earthquake, New Zealand, *Science*, *356*(6334), eaam7194.

Harris, R. A., and S. M. Day (2005), Material contrast does not predict earthquake rupture propagation direction, *Geophysical research letters*, *32*(23).

Hartzell, S. H. (1978), Earthquake aftershocks as Green's functions, *Geophysical Research Letters*, *5*(1), 1–4.

Hartzell, S. H., and T. H. Heaton (1983), Inversion of strong ground motion and teleseismic waveform data for the fault rupture history of the 1979 Imperial Valley, California, earthquake, *Bulletin of the Seismological Society of America*, *73*(6A), 1553–1583.

Hough, S. (1997), Empirical Green's function analysis: Taking the next step, *Journal of Geophysical Research: Solid Earth*, *102*(B3), 5369–5384.

Hutchings, L., and F. Wu (1990), Empirical Green's functions from small earthquakes: a waveform study of locally recorded aftershocks of the 1971 San Fernando earthquake, *Journal of Geophysical Research: Solid Earth*, *95*(B2), 1187–1214.

Iacoletti, S., G. Cremen, and C. Galasso (2021), Advancements in multi-rupture time-dependent seismic hazard modeling, including fault interaction, *Earth-Science Reviews*, *220*, 103,650.

Ishii, M., P. M. Shearer, H. Houston, and J. E. Vidale (2005), Extent, duration and speed of the 2004 Sumatra–Andaman earthquake imaged by the Hi-Net array, *Nature*, *435*(7044), 933–936.

Ji, C., D. J. Wald, and D. V. Helmberger (2002), Source description of the 1999 Hector Mine, California, earthquake, part I: Wavelet domain inversion theory and resolution analysis, *Bulletin of the Seismological Society of America*, *92*(4), 1192–1207.

Jia, Z., and R. W. Clayton (2021), Determination of near surface shear-wave velocities in the central Los Angeles basin with dense arrays, *Journal of Geophysical Research: Solid Earth*, *126*(5), e2020JB021,369.

Jia, Z., X. Wang, and Z. Zhan (2020a), Multifault models of the 2019 Ridgecrest sequence highlight complementary slip and fault junction instability, *Geophysical Research Letters*, *47*(17), e2020GL089,802.

Jia, Z., Z. Shen, Z. Zhan, C. Li, Z. Peng, and M. Gurnis (2020b), The 2018 Fiji Mw 8.2 and 7.9 deep earthquakes: One doublet in two slabs, *Earth and Planetary Science Letters*, *531*, 115,997.

Jia, Z., Z. Jin, M. Marchandon, T. Ulrich, A.-A. Gabriel, W. Fan, P. Shearer, X. Zou, J. Rekoske, F. Bulut, et al. (2023), The complex dynamics of the 2023 Kahramanmaraş, Turkey, M w 7.8-7.7 earthquake doublet, *Science*, *381*(6661), 985–990.

Jin, Z., and Y. Fialko (2020), Finite slip models of the 2019 Ridgecrest earthquake sequence constrained by space geodetic data and aftershock locations, *Bulletin of the Seismological Society of America*, *110*(4), 1660–1679.

Kane, D. L., P. M. Shearer, B. P. Goertz-Allmann, and F. L. Vernon (2013a), Rupture directivity of small earthquakes at Parkfield, *Journal of Geophysical Research: Solid Earth*, *118*(1), 212–221.

Kane, D. L., D. L. Kilb, and F. L. Vernon (2013b), Selecting empirical Green's functions in regions of fault complexity: A study of data from the San Jacinto fault zone, southern California, *Bulletin of the Seismological Society of America*, *103*(2A), 641–650.

Kato, A., S. Sakai, S. Matsumoto, and Y. Iio (2021), Conjugate faulting and structural complexity on the young fault system associated with the 2000 Tottori earthquake, *Communications Earth & Environment*, *2*(1), 13.

Kikuchi, M., and H. Kanamori (1991), Inversion of complex body waves—III, *Bulletin of the Seismological Society of America*, *81*(6), 2335–2350.

Kurzon, I., F. L. Vernon, Y. Ben-Zion, and G. Atkinson (2014), Ground motion prediction equations in the San Jacinto fault zone: Significant effects of rupture directivity and fault zone amplification, *Pure and Applied Geophysics*, *171*, 3045–3081.

Lee, E.-J., P. Chen, and T. H. Jordan (2014), Testing waveform predictions of 3D velocity models against two recent Los Angeles earthquakes, *Seismological Research Letters*, *85*(6), 1275–1284.

Li, X.-Q., and J. L. Nábělek (1999), Deconvolution of teleseismic body waves for enhancing structure beneath a seismometer array, *Bulletin of the Seismological Society of America*, *89*(1), 190–201.

Lin, G. (2020), Waveform cross-correlation relocation and focal mechanisms for the 2019 Ridgecrest earthquake sequence, *Seismological research letters*, *91*(4), 2055–2061.

Luo, Y., Y. Tan, S. Wei, D. Helmberger, Z. Zhan, S. Ni, E. Hauksson, and Y. Chen (2010), Source mechanism and rupture directivity of the 18 May 2009 Mw 4.6 Inglewood, California, earthquake, *Bulletin of the Seismological Society of America*, *100*(6), 3269–3277.

McGuire, J. J., L. Zhao, and T. H. Jordan (2001), Teleseismic inversion for the second degree moments of earthquake space–time distributions, *Geophysical Journal International*, *145*(3), 661–678.

McGuire, J. J., L. Zhao, and T. H. Jordan (2002), Predominance of unilateral rupture for a global catalog of large earthquakes, *Bulletin of the Seismological Society of America*, *92*(8), 3309–3317.

Meng, H., and W. Fan (2021), Immediate foreshocks indicating cascading rupture developments for 527 M 0.9 to 5.4 Ridgecrest earthquakes, *Geophysical Research Letters*, *48*(19), e2021GL095,704.

Monastero, F. C., J. D. Walker, A. M. Katzenstein, and A. E. Sabin (2002), Neogene evolution of the Indian Wells Valley, east-central California, *Geological Society of America Memoirs*, *195*, 199–228.

Mori, J. (1996), Rupture directivity and slip distribution of the M 4.3 foreshock to the 1992 Joshua Tree earthquake, Southern California, *Bulletin of the Seismological Society of America*, *86*(3), 805–810.

Mueller, C. S. (1985), Source pulse enhancement by deconvolution of an empirical Green's function, *Geophysical Research Letters*, *12*(1), 33–36.

Nakahara, H. (2008), Seismogram envelope inversion for high-frequency seismic energy radiation from moderate-to-large earthquakes, *Advances in geophysics*, *50*, 401–426.

Nakahara, H., T. Nishimura, H. Sato, and M. Ohtake (1998), Seismogram envelope inversion for the spatial distribution of high-frequency energy radiation from the earthquake fault: Application to the 1994 far east off Sanriku earthquake, Japan, *Journal of Geophysical Research: Solid Earth*, *103*(B1), 855–867.

Nielsen, S. B., and L. Knopoff (1998), The equivalent strength of geometrical barriers to earthquakes, *Journal of Geophysical Research: Solid Earth*, *103*(B5), 9953–9965.

Nissen, E., J. Elliott, R. Sloan, T. Craig, G. Funning, A. Hutko, B. Parsons, and T. Wright (2016), Limitations of rupture forecasting exposed by instantaneously triggered earthquake doublet, *Nature Geoscience*, *9*(4), 330–336.

Ross, Z. E., C. Rollins, E. S. Cochran, E. Hauksson, J.-P. Avouac, and Y. Ben-Zion (2017), Aftershocks driven by afterslip and fluid pressure sweeping through a fault-fracture mesh, *Geophysical Research Letters*, *44*(16), 8260–8267.

Ross, Z. E., B. Idini, Z. Jia, O. L. Stephenson, M. Zhong, X. Wang, Z. Zhan, M. Simons, E. J. Fielding, S.-H. Yun, et al. (2019), Hierarchical interlocked orthogonal faulting in the 2019 Ridgecrest earthquake sequence, *Science*, *366*(6463), 346–351.

Sato, H., M. C. Fehler, and T. Maeda (2012), *Seismic wave propagation and scattering in the heterogeneous earth*, vol. 496, Springer.

Schwartz, D. P., P. J. Haeussler, G. G. Seitz, and T. E. Dawson (2012), Why the 2002 Denali fault rupture propagated onto the Totschunda fault: Implications for fault branching and seismic hazards, *Journal of Geophysical Research: Solid Earth*, *117*(B11).

Shearer, P. M., R. E. Abercrombie, and D. T. Trugman (2022), Improved stress drop estimates for M 1.5 to 4 earthquakes in southern California from 1996 to 2019, *Journal of Geophysical Research: Solid Earth*, *127*(7), e2022JB024,243.

Shelly, D. R. (2020), A high-resolution seismic catalog for the initial 2019 Ridgecrest earthquake sequence: Foreshocks, aftershocks, and faulting complexity, *Seismological Research Letters*, *91*(4), 1971–1978.

Somerville, P. G., N. F. Smith, R. W. Graves, and N. A. Abrahamson (1997), Modification of empirical strong ground motion attenuation relations to include the amplitude and duration effects of rupture directivity, *Seismological research letters*, *68*(1), 199–222.

Tan, Y., and D. Helmberger (2010), Rupture directivity characteristics of the 2003 Big Bear sequence, *Bulletin of the Seismological Society of America*, *100*(3), 1089–1106.

Thakur, P., and Y. Huang (2021), Influence of fault zone maturity on fully dynamic earthquake cycles, *Geophysical Research Letters*, *48*(17), e2021GL094,679.

Toda, S., and R. Stein (2003), Toggling of seismicity by the 1997 Kagoshima earthquake couplet: A demonstration of time-dependent stress transfer, *Journal of Geophysical Research: Solid Earth*, *108*(B12).

Vallée, M. (2004), Stabilizing the empirical Green function analysis: Development of the projected Landweber method, *Bulletin of the Seismological Society of America*, *94*(2),

394–409.
Vallée, M., J. Charléty, A. M. Ferreira, B. Delouis, and J. Vergoz (2011), SCARDEC: a new technique for the rapid determination of seismic moment magnitude, focal mechanism and source time functions for large earthquakes using body-wave deconvolution, *Geophysical Journal International*, *184*(1), 338–358.
Wang, E., and A. M. Rubin (2011), Rupture directivity of microearthquakes on the San Andreas Fault from spectral ratio inversion, *Geophysical Journal International*, *186*(2), 852–866.
Wang, K., D. S. Dreger, E. Tinti, R. Bürgmann, and T. Taira (2020), Rupture process of the 2019 Ridgecrest, California M w 6.4 foreshock and M w 7.1 earthquake constrained by seismic and geodetic data, *Bulletin of the Seismological Society of America*, *110*(4), 1603–1626.
Wang, T., S. Wei, X. Shi, Q. Qiu, L. Li, D. Peng, R. J. Weldon, and S. Barbot (2018), The 2016 Kaikōura earthquake: Simultaneous rupture of the subduction interface and overlying faults, *Earth and Planetary Science Letters*, *482*, 44–51.
Wang, X., and Z. Zhan (2020), Seismotectonics and fault geometries of the 2019 Ridgecrest sequence: Insight from aftershock moment tensor catalog using 3-D Green's functions, *Journal of Geophysical Research: Solid Earth*, *125*(5), e2020JB019,577.
Wang, X., L. Chen, and Q.-F. Chen (2024), Evaluation of 3D crustal seismic velocity models in southwest China: Model performance, limitation, and prospects, *Science China Earth Sciences*, pp. 1–16.
Warren, L. M., and P. M. Shearer (2006), Systematic determination of earthquake rupture directivity and fault planes from analysis of long-period P-wave spectra, *Geophysical Journal International*, *164*(1), 46–62.
Wessel, P., W. H. Smith, R. Scharroo, J. Luis, and F. Wobbe (2013), Generic mapping tools: improved version released, *Eos, Transactions American Geophysical Union*, *94*(45), 409–410.
White, M. C., H. Fang, R. D. Catchings, M. R. Goldman, J. H. Steidl, and Y. Ben-Zion (2021), Detailed traveltime tomography and seismic catalogue around the 2019 M w7. 1 Ridgecrest, California, earthquake using dense rapid-response seismic data, *Geophysical Journal International*, *227*(1), 204–227.
Wu, R.-S., J. Luo, and B. Wu (2014), Seismic envelope inversion and modulation signal model, *Geophysics*, *79*(3), WA13–WA24.
Xu, S., E. Fukuyama, F. Yamashita, H. Kawakata, K. Mizoguchi, and S. Takizawa (2023), Fault strength and rupture process controlled by fault surface topography, *Nature Geoscience*, *16*(1), 94–100.
Yoshida, K., N. Uchida, H. Kubo, R. Takagi, and S. Xu (2022), Prevalence of updip rupture propagation in interplate earthquakes along the Japan Trench, *Earth and Planetary Science Letters*, *578*, 117,306.
Zaliapin, I., and Y. Ben-Zion (2011), Asymmetric distribution of aftershocks on large faults in California, *Geophysical Journal International*, *185*(3), 1288–1304.
Zielke, O., M. Galis, and P. M. Mai (2017), Fault roughness and strength heterogeneity control earthquake size and stress drop, *Geophysical Research Letters*, *44*(2), 777–783.